Annales
Geophysicae
Discussions

Sounding of sporadic E layers from CSES radio occultation and comparing with ionosonde measurements

Chengkun Gan[1], Jiayu Hu[2] , Xiaomin Luo[3], Chao Xiong[4,5], Shengfeng Gu[1]

[1]GNSS Research Center, Wuhan University, Wuhan 430079, China
5   [2]School of Geodesy and Geomatics, Wuhan University, Wuhan 430079, China
[3]School of Geography and Information Engineering, China University of Geosciences (Wuhan), Wuhan 430074, China
[4]Department of Space Physics, School of Electronic Information, Wuhan University, Wuhan 430072, China
[5]Hubei Luojia Laboratory, Wuhan 430079, China

Correspondence to: Shengfeng Gu (gsf@whu.edu.cn)

10   **Abstract.** GNSS radio occultation (RO) plays an important role in ionospheric electron density inversion and sounding of sporadic E layers. As the China's first electromagnetic satellite, China Seismo Electromagnetic Satellite (CSES) has collected the RO data from both GPS and BDS-2 satellites since March 2018. In this study, we extracted the carrier to noise density ratio (CNR) data of CSES and calculated the standard deviation of normalized CNR. A new criterion is developed to determine the Es events, that is when the mean value of the absolute value of the difference between the normalized CNR is

15   greater than 3 times of the standard deviation. The statistics show that sporadic E layers have strong seasonal variations with highest occurrence rates in summer season at middle latitudes. It is also found that the occurrence height of Es is mainly located at 90-110 km, and the period of local time 15:00-18:00 is the high incidence period of Es. In addition, the geometric altitudes of a sporadic E layer detected in CSES radio occultation profiles and the virtual heights of a sporadic E layer obtained by the Wuhan Zuo Ling Tai (ZLT) ionosonde show four different space-time matching criterions. Our results reveal

20   that there is a good agreement between both parameters which is reflected in the significant correlation.

1. Introduction

The name Sporadic E and its abbreviation Es refer to thin layers of metallic ion plasma which accumulates in the dynamo region of the Earth's ionosphere, mostly between 100 and 125 km, where ion motion is controlled mainly by collisions with the neutrals, thus the ions move with the winds while electrons remain strongly magnetized (Haldoupis 2012). The formation

25   of sporadic E layer was traditionally attributed to the "windshear theory" (Whitehead 1961; Axford 1963; Whitehead 1989), in which vertical shears in the horizontal wind play a key role in forming these layers from long-lived metallic ions through ion-neutral collisional coupling and geomagnetic Lorentz forcing, vertical shear converge metallic ions into thin sheets of enhanced electron density. More recently, researchers have found multiple factors can contribute to the occurrence of Es, including tidal wind, the Earth's geomagnetic field, and meteoric deposition of metallic material in the background

30   thermosphere, resulting in variations of Es occurrence with respect to local time, altitude, latitude, longitude, and season

(Haldoupis, 2011; Yeh et al, 2014, Didebulidze et al., 2020). Meanwhile, the ionospheric E region has a relatively higher electrical conductivity and therefore plays a crucial role in the ionosphere electron dynamics at both E- and F-region altitudes (Yue et al. 2015).

35   Variance in the signal to noise ratio (SNR) caused by strong gradients in the index of refraction has been suggested to identify and sound sporadic E layers (Wu et al., 2005; Arras et al., 2008; Yeh et al., 2012; Hocke et al., 2001; Yue et al., 2015; Tsai et al. 2018). However, in terms of judgment criteria, many scholars propose different selection methods. Chu (2014) set thresholds for signal phase amplitude and carrier phase delay ratio when screening Es, and the ratio of disturbance amplitude to normalized SNR must be greater than 0.01 then it can be counted as Es event. Wu et al. (2005) directly used the
40   normalized SNR data sequence as the characteristic parameter to detect Es. Arras et al. (2017) and Tsai et al. (2018) used the value of 0.2 as the threshold of the normalized SNR standard deviation sequence. It is considered that Es event occurs when the peak exceeds 0.2. Xue et al. (2018) used 0.1 as the standard deviation threshold to detect single-layer and multi-layer Es events at the same time. Based on GPS radio occultation (RO) techniques, some investigations established global distribution of Es layers information to analyze the climatology of global Es occurrence rates. (Arras et al., 2008; Wickert et al., 2004;
45   Yeh et al., 2012; Tilo et al., 2014; Arras et al. 2017).

Since the invention of ionosonde in the nineteen thirties, Es has been investigated extensively from ground, by means of analyzing ionosonde and incoherent scatter radar observations (Whitehead 1989; Mathews 1998). Ionosondes provide reliable measurements on sporadic E parameters and on the altitude of each layer. The altitudes are given in virtual heights,
50   and the lower boundary of the sporadic E layer (h'Es). Arras et al. (2017) compared sporadic E altitudes and their intensity with ground based ionosonde data provided by the Digisonde located at Pruhonice close to Prague, Czech Republic (geographic 50°N, 14.5°E) to confirm the derived sporadic E parameters. Wuhan Zuo Ling Tai (ZLT) ionosonde (geographic 30.5°N, 114.4°E) is located in central China. It is a representative location due to its low geomagnetic latitude and the longest observational record, which has been well-maintained during the past several decades and its data are of high quality
55   (Zhou et al. 2021).

China's first electromagnetic satellite, China Seismo Electromagnetic Satellite (CSES), also known as ZH01(01), was successfully launched on Feb 2, 2018 (Shen et al. 2018). In recent years, a few studies were published concerning the performance of different payloads of CSES. Ambrosi et al. (2018) investigated the seismo-associated perturbations of the
60   Van Allen belts using the High Energetic Particle Detector (HEPD) of the CSES satellite mission. Concerning the performance of the Electric Field Detector (EFD) on board, Huang et al. (2018) studied several natural electromagnetic emissions during the six-month orbit test phase, and the preliminary analysis suggested that the EFD show good performance. Cao et al. (2018) studied the data from the search coil magnetometer (SCM) mounted on CSES that designed to measure the magnetic field fluctuation of low frequency electromagnetic waves ranging from 10 Hz to 20 kHz, they concluded that the

65   performance of SCM can satisfy the requirement of scientific objectives of CSES mission. As one of the main payloads, the GNSS occultation receiver (GOR) had the occultation observation function of both GPS and BDS-2 (Lin et al. 2018). Yan et al. (2020) provided a comprehensive comparison of in situ electron density (Ne) and temperature (Te) measured by Langmuir probe (LAP) on board the CSES with other space-borne and ground-based observations. Their results suggested that the CSES in situ plasma parameters are reliable with a high scientific potential for investigation of geophysics and space.

70   Wang et al. (2019) compared CSES ionospheric RO data with Constellation Observing System for Meteorology, Ionosphere and Climate (COSMIC) measurements. Results indicated that NmF2 and hmF2 between CSES and COSMIC is in extremely good agreement, and co-located electron density profiles (EDPs) between the two sets are generally in good agreement above 200 km.

75   Though the performance of CSES has already been analyzed for different payloads, there are still rooms for an in-depth analysis of GOR, especially for the region with an altitude below 200 km, e.g., E-layer. In addition, as demonstrated by previous studies, the RO measurements can provide a very valuable data for the global sounding of sporadic E layers. In this study we assessed the GRO performance of CSES in the investigating of lower ionosphere, especially the occurrence and properties of sporadic E layers on a global scale.

80

This paper is organized as follows. We first realize the algorithm of sounding sporadic E layers with almost nine months CSES GOR data. Then, we show the results and discussions on global Es-event morphology. Afterward, the comparison of Es altitudes from RO profiles with those from Wuhan ZLT ionosonde measurements reveal a large correspondence between both measurement techniques are introduced. Finally, we present the conclusion.

85   **2. Methods**

Based on GNSS RINEX format data, we first calculates the electron density profile by occultation inversion algorithm (Lei et al, 2007; Yue et al, 2011), then extracts the carrier to noise density ratio (CNR) data of L1 and the corresponding time information according to the observation data. Considering the resolution of time and altitude, moving average of 31 points (corresponding to 70-120 km in the vertical direction) is used to calculate the background trend term of CNR data. After that,

90   we calculate the normalized CNR data and the standard deviation of normalized CNR data. A new criterion is developed to determine whether Es occurs. That is, when the mean value of the absolute value of the difference between the normalized CNR is greater than 3 times the standard deviation, we consider the Es occurs. If more than one value of the normalized CNR sequence meets the conditions, multi-layer Es occurs.

2.1 Sounding of sporadic E layers

95 Carrier to noise ratio, denoted as CNR or C/N (dB-Hz), provides highly desirable information about the quality of the received GNSS signal. Signal to noise ratio, denoted as SNR, is directly related to the C/N measurement and the coherent integration time T_{coh} as,

$$C/N = 10\log_{10}(\frac{SNR}{T_{coh}}) \tag{1}$$

where the coherent integration time T_{coh} is used to compute the cross-ambiguity function (CAF) as the most effective way to

100 detect weak signals in traditional receivers. The T_{coh} is a known parameter since it is chosen by the receiver. We only need to estimate SNR to obtain the C/N measurement (Gómez et al. 2018). The SNR is very sensitive to the electron density changing with altitude, e.g., the sporadic E layer. These vertically small variations in the electron density would lead to phase fluctuation of the GNSS signal which can be observed as a reduction or increase of the signal power at the receiver (Hajj et al., 2002). According to Equation (1), C/N and SNR have the same trend, which can indicate the quality of

105 observation signal, therefore, we can apply C/N data instead of SNR data for sounding of sporadic E layers.

Because CNR data itself also has a certain long-term variation, we need to extract the background trend item in CNR data to obtain the disturbance information after removing the background trend. In this study, the moving average method is used to extract the background trend term of CNR data. The formula is as follows:

110 $$\overline{X_k} = \frac{X_{k-\frac{N-1}{2}}+\cdots+X_k+\cdots+X_{k+\frac{N-1}{2}}}{N} \tag{2}$$

where, X_k and $\overline{X_k}$ is the k-th data of the original CNR sequence and after smoothing, and N is the size of the smoothing window. Considering that the original data processed in this study is the original occultation observation data with a sampling rate of 1Hz, so we choose 31 data points as the size of the smooth window.

115 It is inconvenient to analyze CNR data due to the large value of CNR data, therefore, it has to be first normalized. The calculation formula is as follows:

$$CNR1 = \frac{CNR}{CNR0} \tag{3}$$

where CNR is the original data sequence, CNR0 is the background trend item sequence, and CNR1 is the normalized data sequence.

120

Note that there is no strict standard to judge whether single-layer Es or multi-layer Es occurs. In this study, 70-120 km is selected as the interval to sound the occurrence of Es events. The standard deviation of normalized CNR sequence is calculated:

$$\overline{CNR1} = \sum_{i=1}^{n} CNR1_i \tag{4}$$

125 $$std = \sqrt{\sum_{i=1}^{n}(CNR1_i - \overline{CNR1})^2/(n-1)}$$ (5)

where $\overline{CNR1}$ is the normalized CNR sequence mean; $CNR1_i$ is the normalized CNR sequence; n is the number of normalized CNR sequences. It is thought that Es occurred once the difference of $CNR1_i$ from the mean is greater than 3 times the standard deviation. While there are multi-layer Es occurs in a single occultation event if multiple $CNR1_i$ meets the judgment criteria.

130

We selected two representative occultation events from CSES observation data as examples to verify the correctness of our Es detection algorithm. The detection of single-layer Es event is shown in Figure 1. The left figure shows the electron density profile of G06 satellite at 06:56UT on August 14, 2018 and the CNR profile. The right figure shows the electron density profile, normalized CNR profile within 60-160 km at the same time, in which the red dotted line is $\overline{CNR1} \pm 3std$

135 boundary vertical line, it can be seen that there is a $CNR1_i$ whose value exceeds the boundary line and corresponds to the height of abnormal electron density in the figure. According to the normalized CNR sequence, the Es height detected in the figure is 96.49 km. The detection of multi-layer Es events is shown in Figure 2. The left figure shows the electron density profile and the CNR profile of G17 satellite at 20:58 on August 27, 2018. The right figure shows the electron density profile, normalized CNR profile within 60-160 km at the same time. The red dotted line is $\overline{CNR1} \pm 3std$ boundary vertical line, and

140 the Es heights detected in the figure are 73.63 km and 102.76 km respectively.

The principle of occultation inversion is based on the spherical symmetry assumption. There is a certain deviation in the low altitude range, and the electron density calculated by inversion will also have an impact. Compared with the electron density itself, the signal-to-noise radio is more sensitive to the electron density gradient, the SNR peak height does not fully correspond to the local peak of electron density, and the CNR data does not fully correspond, Therefore, it will affect the

145 inversion height comparison. Arras et al (2017) also obtained that there is a deviation between the height of Es layer and the peak height of electron density.
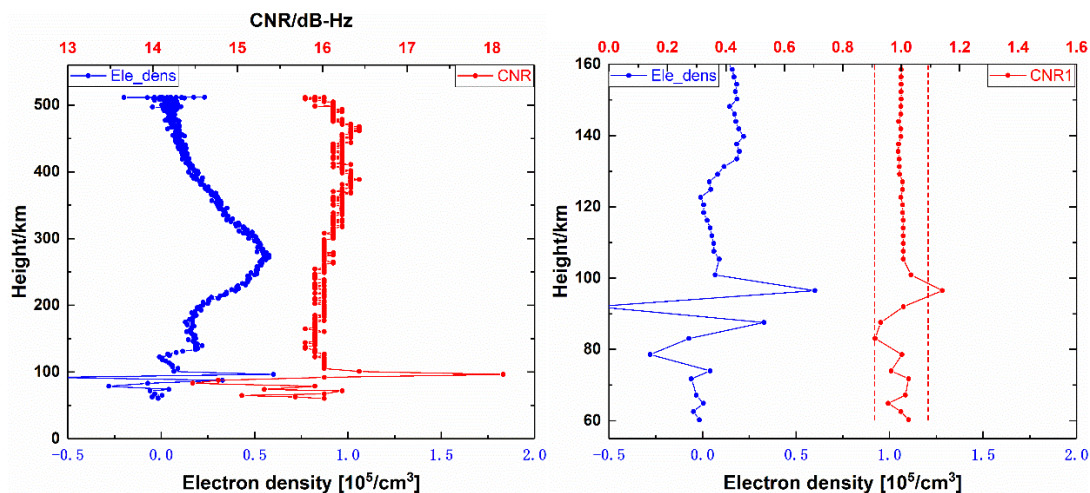
Figure 1 Schematic diagram of G06 single-layer Es sounding. The left figure shows the electron density profile of G06 occultation event and the CNR profile at 06:56 on August 14, 2018, the right figure shows the electron density profile and normalized CNR profile within 60-160 km at the same time, and the red dotted line is $\overline{CNR1} \pm 3std$ boundary vertical.
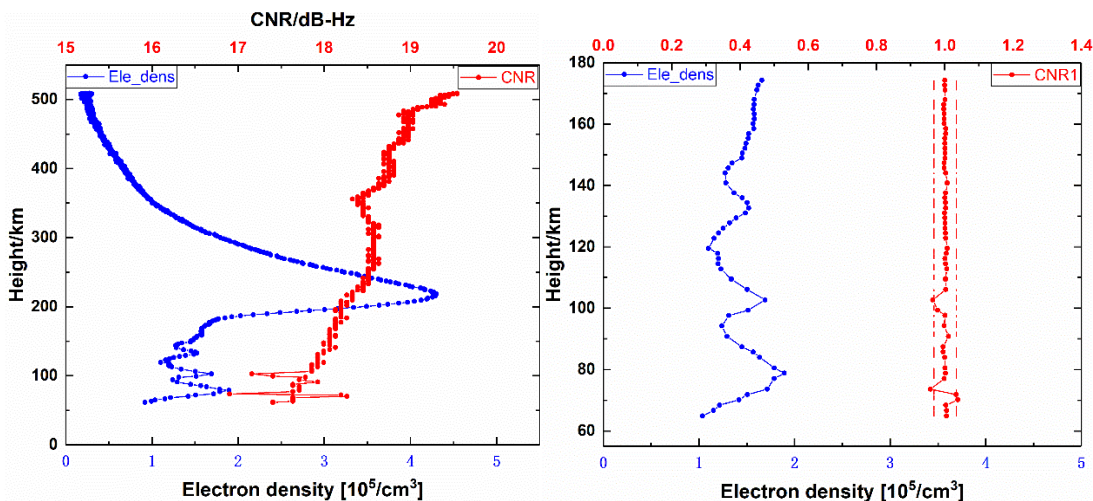
Figure 2 Schematic diagram of G17 multi-layer Es sounding. The left figure shows the electron density profile of G17 occultation event and the CNR profile at 06:56 on August 14, 2018, the right figure shows the electron density profile and normalized CNR profile within 60-160 km at the same time, and the red dotted line is $\overline{CNR1} \pm 3std$ boundary vertical.

3. Discussions on global Es-event morphology

The GOR measurement of CSES from March 1 to December 1 in 2018 are used in the data analysis. With nearly nine months of data from CSES, there are 104531 and 12642 electron density profiles obtained from GPS and BDS-2 data of CSES, respectively. The inversion algorithm is utilized based on the FUSING (FUSing IN Gnss) software (Shi et al. 2018;

160   Zhao et al. 2018; Gu et al. 2020; Gu et al. 2021). Originally, the FUSING software is developed for high precision real-time GNSS data processing and multi-sensor navigation, and now it can also be used for atmospheric modeling (Lou et al. 2019; Luo et al. 2020; Luo et al. 2021).

3.1 Distribution of Es occurrence rate for seasons and altitude

The nine-month data have been divided into spring (March, April and May), summer (June, July and August) and autumn
165   (September, October and November). For each season, we use the altitude resolution of 1 km to count the number of occultation events which sound Es events in each altitude interval. Due to the resolution of observation values, we do not distinguish the occultation events of sounding Es in different layers. Considering the error caused by the integrity of the original observation data in different seasons and different days, we count the total number of days with observation data in each season, then calculate the ratio of the number of occultation events with Es events in different height intervals to the
170   total number of days in the season, that is counting the number of occultation events with Es events per day. Since CSES has both GPS and BDS-2 observations, we count the average number of daily occultation events which sound Es events of different satellite systems. The results are as follows:
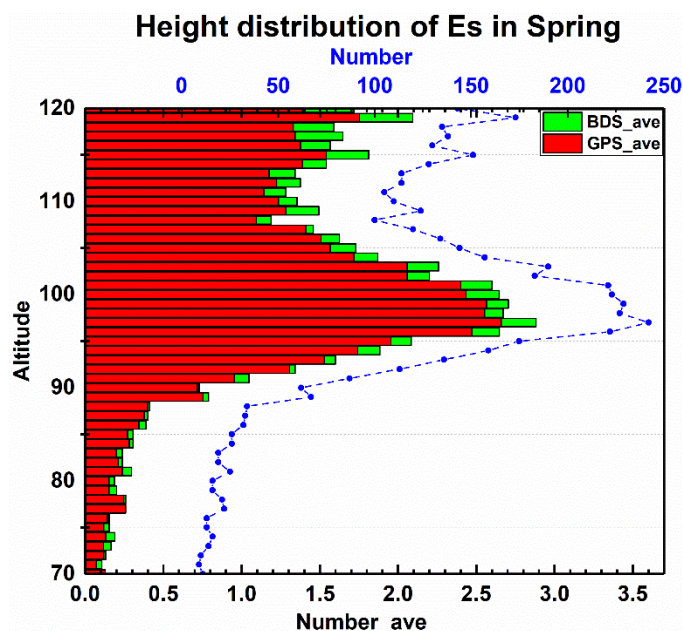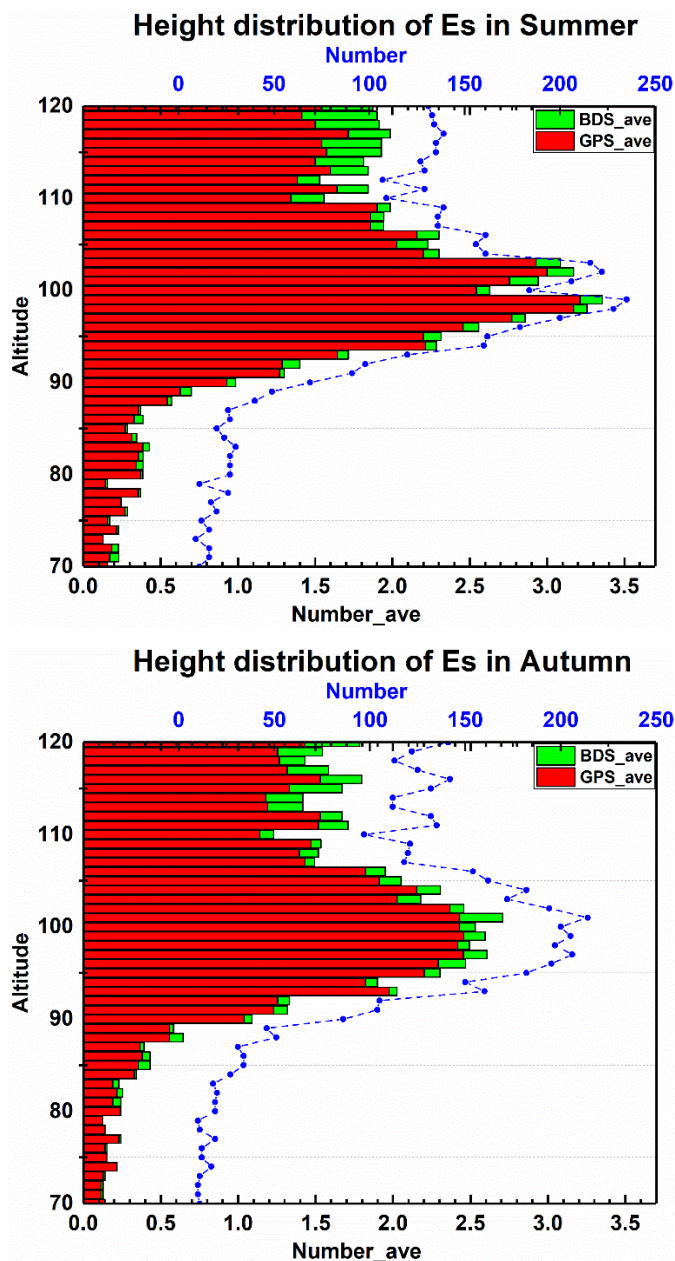
Figure. 3 Height distribution of Es average daily occurrence rate for three different seasons, from top to bottom are the results with spring, summer and autumn, respectively. The blue dotted line diagram shows the total number of occultation events with Es, the red and green bar chart shows the number of occultation events with Es events per day.
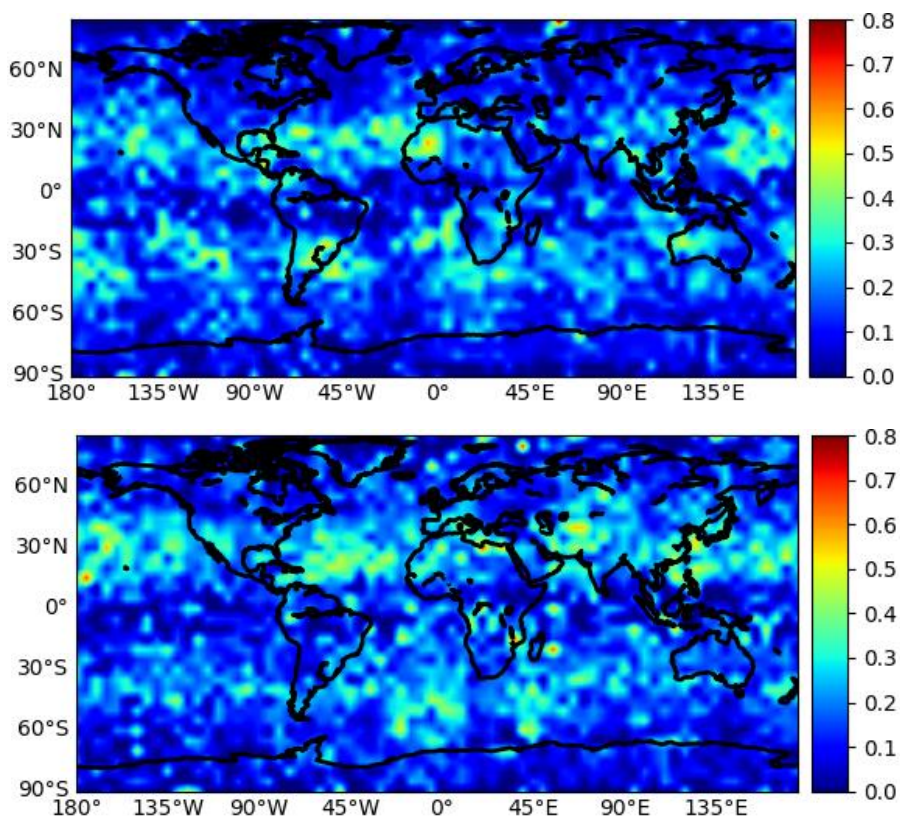
There are the results with spring, summer and autumn from top to bottom, respectively. It can be seen from Fig. 3 that the Es average daily occurrence rate has obvious seasonal variation, the height of Es occurrence in spring, summer and autumn is

mainly 90-110 km, the height with the largest daily average incidence of Es in spring is 98 km, with a daily average of 2.88, the height with the largest daily average incidence in summer is 99 km, with a daily average of 3.36, and in autumn the height is 101 km, with a daily average of 2.71. The lower total number of occultation events with Es in summer is due to the lack of observation data of CSES for about 20 days in summer. The results show overall distribution of three seasons shifts to a slightly higher height, and more Es also appears above 110 km. The reasons, firstly, there are less observation data of CSES at lower altitude, and this situation is reflected in the blue dotted line diagram of Fig. 3; secondly, due to the time resolution, some initial lower altitude values are discarded when using the sliding window to calculate the CNR background trend term, Es occurring at a lower height is also discarded at the same time.

3.2 Distribution of global Es occurrence rate for seasons

The global longitude and latitude regions are divided into grids with a resolution of 5°×5°. The number of occultation events in each grid and the number of occultation events with Es events are counted, and the ratio of the number of occultation events with Es to the total number of occultation observations is taken as the Es occurrence frequency of the grid. Finally, the global longitude-latitude distribution characteristics of Es occurrence frequency in this season are obtained. The statistical results are as follows:
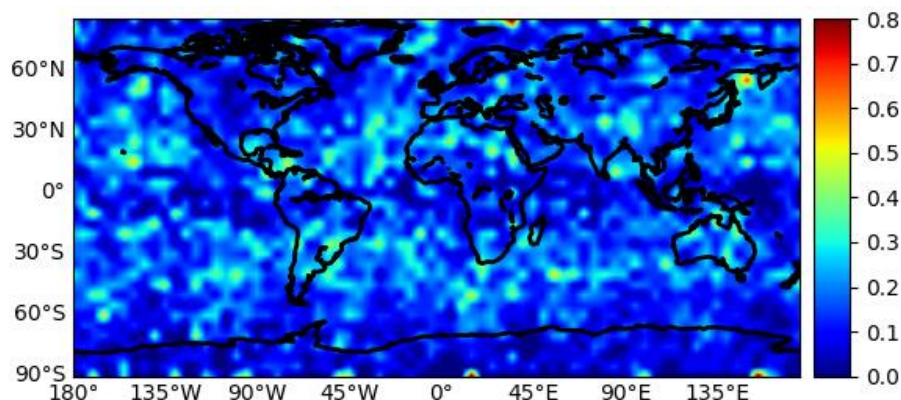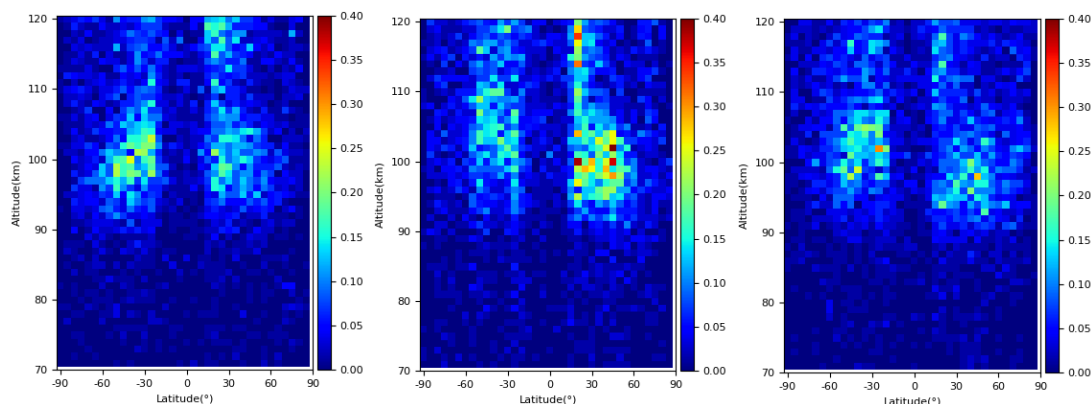
Figure 4 The geographical distribution of Es occurrence rate for three different seasons in 5°×5° geographic latitude/longitude grid, from top to bottom are the results with spring, summer and autumn, respectively.

There are the results with spring, summer and autumn from top to bottom, respectively. In general, Es preferably occurs at midlatitudes of the summer hemisphere. The overall occurrence frequency of global Es in spring and autumn is lower than that in summer. This phenomenon may be due to the strong solar radiation in summer and the ionization of more metal atoms in the ionosphere, which increases the source of Es and promotes the formation of Es. Therefore, the occurrence rate in mid-latitude of the hemisphere in summer is higher than that in other latitudes (Chu et al. 2014). There is no significant difference in the frequency of Es between the northern and southern hemispheres in spring and autumn, and it shows an almost symmetrical trend along the equator. In spring and autumn, the direct point of the sun is near the equator. Because the magnetic line of force here is almost horizontal, it is difficult to form ion aggregation even if the ionization rate increases, so the occurrence rate is relatively high in the low latitude area of the magnetic equator (Arras et al. 2017; Xue et al. 2018). The Es rates at polar regions are always low. We can also find an occurrence depression around the American area (the longitude sector of 70°–120° W) in the mid-latitude in summer, where the Es occurrence rates were lower than anywhere else along the zone bands, this is consistent with the phenomenon found by Tsai et al. 2018.

3.3 Distribution of Es occurrence rate for latitude and altitude

To comprehensively analyze the distribution of Es incidence with latitude and altitude, the latitude-altitude region is divided into grids with a resolution of 5°×1km. Similarly, the ratio of the number of occultation events corresponding to Es events in the grid to the total number of days with observed data in the season is calculated, the daily average number of Es events is taken as the occurrence frequency of Es for statistical analysis. The results are as follows:
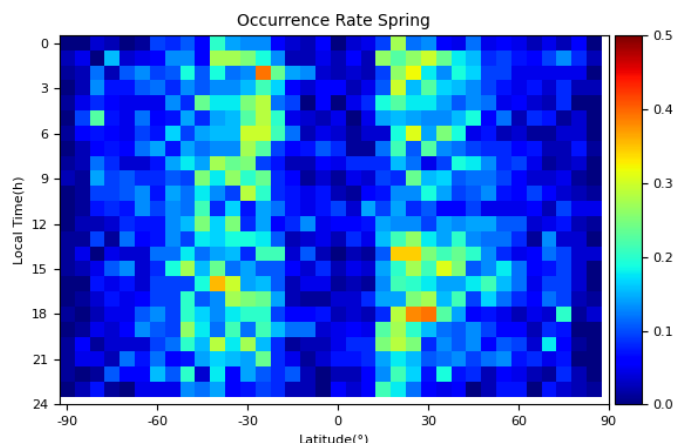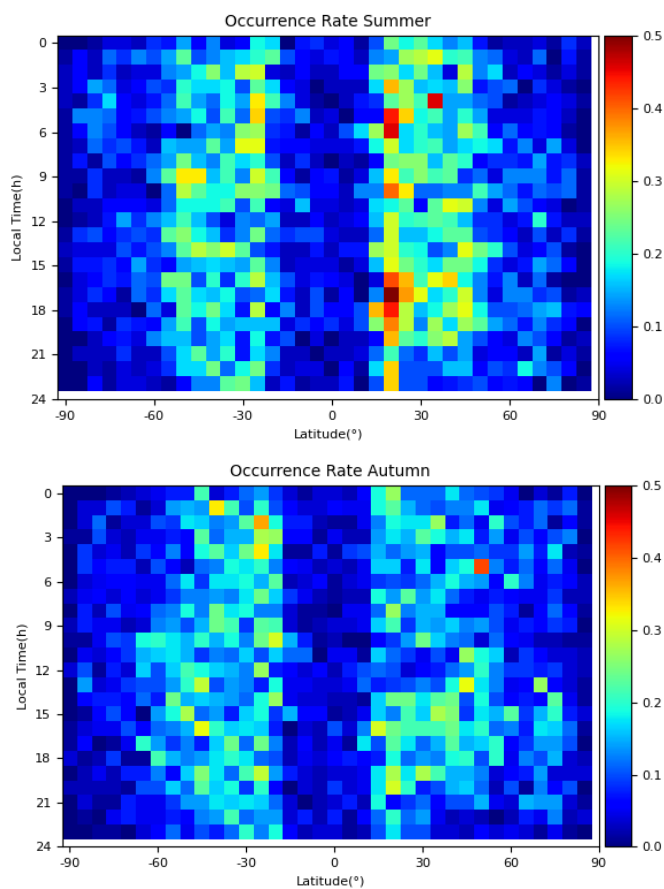
220 **Figure 5 The distribution of Es occurrence rate for three different seasons in 5°×1km geographic latitude/altitude grid, from left to right are the results with spring, summer and autumn, respectively.**

There are the results with spring, summer and autumn from left to right, respectively. It can be seen from the figure that the incidence of Es latitude altitude shows obvious seasonal changes. The incidence of Es in summer in the northern hemisphere 225 is significantly higher than that in spring and autumn in the same latitude range and height range. The latitude range of Es high incidence is 20°-50° north-south latitude, mainly around 30°. The occurrence height of Es is mainly concentrated in 90-110 km.

3.4 Distribution of Es occurrence rate for local time and latitude

In order to comprehensively analyze the distribution of Es incidence with local time and latitude, the local-time-latitude 230 region is divided into grids with a resolution of 1h × 5°. Similarly, the ratio of the number of occultation events corresponding to Es events in the grid to the total number of days with observed data in the season is calculated, the daily average number of Es events is taken as the occurrence frequency of Es for statistical analysis. The results are as follows:

Figure 6 The distribution of Es occurrence rate for three different seasons in 1h×5° local time/geographic latitude grid, from top to bottom are the results with spring, summer and autumn, respectively.

There are the results with spring, summer and autumn from top to bottom, respectively. It can be seen from the figure that the incidence of Es shows obvious local time changes, the period of local time 15:00-18:00 is the high incidence period of Es in all seasons. This is because the occurrence of Es is directly related to the intensity of solar radiation, the electricity and aggregation of metal ions gradually occur, therefore, there is a delay between the high incidence period of Es and the 12:00 of local time with the strongest solar radiation.

4. Experiments of Comparing with Ionosonde measurements

In this study, we choose a certain space-time matching criterion to obtain the pairs of the geometric altitudes of a sporadic E layer detected in CSES radio occultation profiles and the virtual heights of a sporadic E layer obtained by the ZLT ionosonde for confirming the derived sporadic E parameter in height. Luo et al. (2019) choose a certain space-time matching criterion to evaluate the quality of the electron density profile from the FY-3C mission with respect to COSMIC mission. We

Annales
Geophysicae
Discussions

Open Access

EGU

modified their method to confirm the height of the derived sporadic E layer. We counted the data of Wuhan ZLT ionosonde

250 from March 1 to December 16 in 2018 of the same period, and extracted the h'Es data. The space-time matching criterion is quantified as the size of the space-time window centered on the position and occurrence time of the sporadic E layer obtained by the ZLT ionosonde. The sporadic E layer detected in CSES radio occultation profiles falling into the space-time window and the sporadic E layer obtained by the ZLT ionosonde constitute the pairs participating in the comparative analysis. Here the space-time window is denoted as (B, L, T), where B and L represent the size of space window along

255 latitude and longitude, respectively; T represents the size of the time window.

In this study, considering that the temporal resolution of the ionosonde is 15 minutes, four different space-time matching criteria are proposed with the window as (10°, 10°, 7.5 min), (5°, 10°, 7.5min), (5°, 5°, 7.5min) and (2°, 5°, 7.5min), respectively. Among the other parameters, the height of sporadic E layer is an important parameter of the derived sporadic E

260 layer. Thus, the correlation coefficient (CC), is derived for determining the height of sporadic E layer. The definition of the correlation coefficient is presented below.

$$CC = \frac{\sum_{i=1}^{N}(X_i^C \cdot X_i^Z) - \frac{1}{N}\sum_{i=1}^{N}X_i^C \sum_{i=1}^{N}X_i^Z}{\sqrt{\left(\sum_{i=1}^{N}(X_i^C)^2 - \frac{1}{N}(\sum_{i=1}^{N}X_i^C)^2\right)\left(\sum_{i=1}^{N}(X_i^Z)^2 - \frac{1}{N}(\sum_{i=1}^{N}X_i^Z)^2\right)}} \tag{6}$$

where N represents the total number of data pairs in the matching group under a given spatiotemporal matching windows; X_i^C (i=1,2,3···,n) represents the geometric altitudes of ith sporadic E layer detected in CSES radio occultation profiles;

265 X_i^Z (i=1,2,3···,n) represents the virtual heights of ith sporadic E layer obtained by the ZLT ionosonde.

Figure 7 shows an example of simultaneous detecting Es by CSES and ZLT ionosonde，the left figure shows the electron density profile of G13 satellite at 07:02 on August 15, 2018 and the electron density profile of ZLT ionosonde at 07:00 on August 15, 2018, the right figure shows the electron density profile in the range of 0-200 km. In the figure, the geodetic

270 coordinates of Es detected by CSES is (39.5°N, 115.2°E,102.990 km) and the geodetic coordinates of Es detected by ZLT is (30.5°N, 114.4°E, 102.994 km).
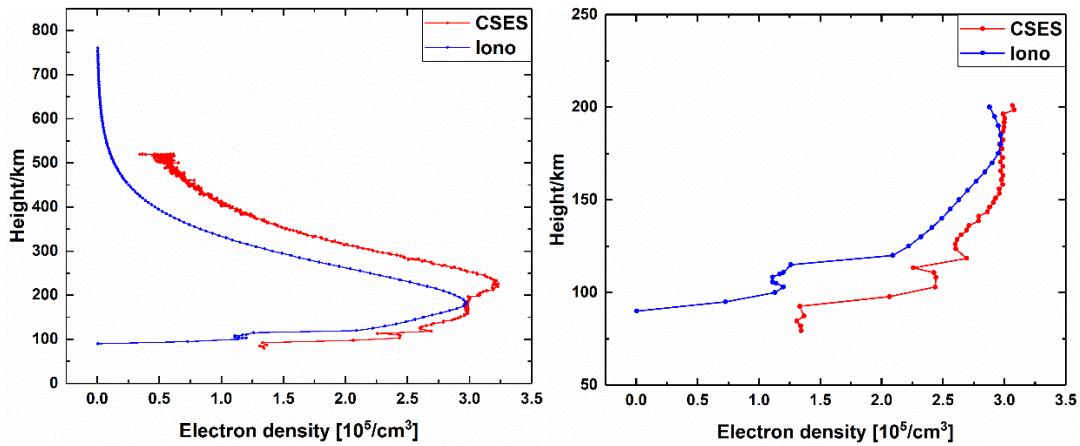
Figure 7 An example of simultaneous detecting Es by CSES and ZLT ionosonde, the left figure shows the electron density profile of G13 satellite at 07:02 and ZLT ionosonde at 07:00 on August 15, 2018, the right figure shows the electron density profile in the range of 0-200 km.

Figure 8 presents the comparison of the geometric altitudes of a sporadic E layer detected in CSES radio occultation profiles and the virtual heights of a sporadic E layer obtained by the ZLT ionosonde. In the fourth subgraph, there are two points at 111.25 km of the ionosonde data, corresponding to 106.37 km and 106.40 km of CSES data respectively, with small difference and almost overlapping in the figure. These figures reveals that there is a good agreement between both parameters, which can also be seen from the high correlation larger than 0.7. The comparison among different windows conclude that the correlation increased slightly as a stricter space-time matching window involved, but with less pairs or couples. Compared with results from Arras et al. (2018), we also found a height offset between both measurement techniques at 100-110 km altitude. This may result from the different height parameters used for both techniques: the geometric heights provided by the RO technique and the virtual height which is influenced by the ionization below the sporadic E layer calculated from ionosonde recordings (Arras et al. 2018).
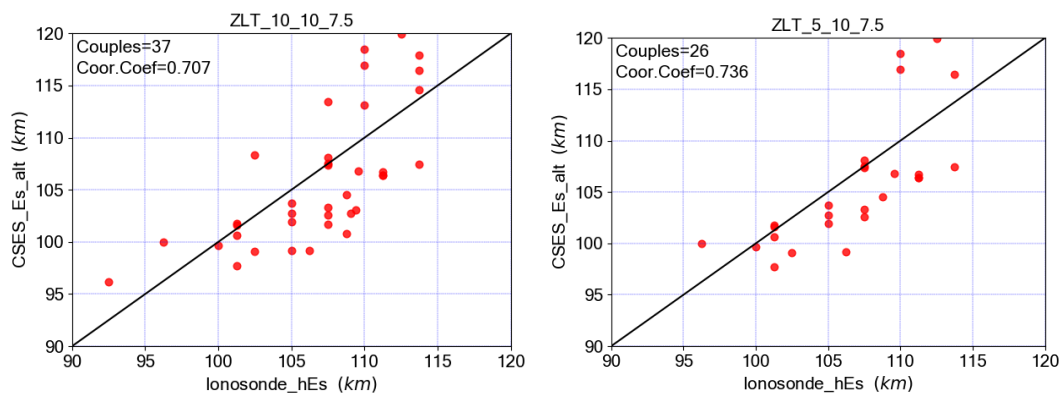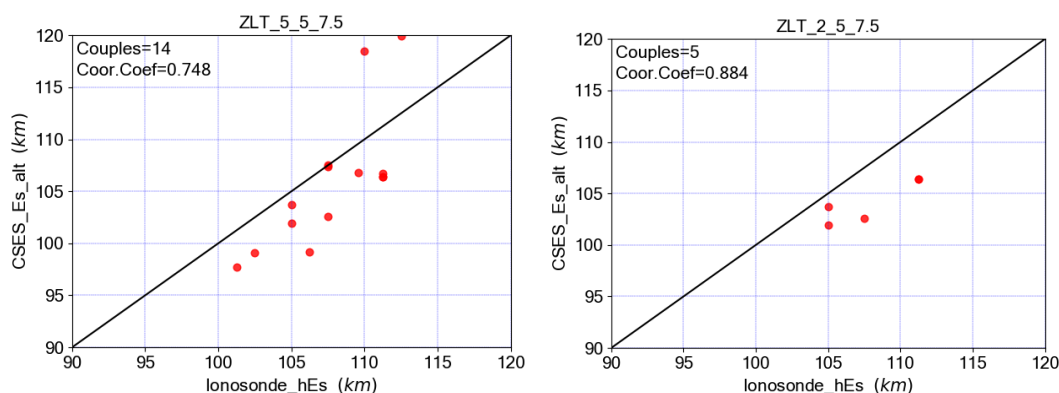
Figure 8 Comparison of the geometric altitudes of Es detected in CSES radio occultation profiles and the virtual heights of Es obtained by the ZLT ionosonde. From top to bottom and from left to right are the results with space-time matching window (10°, 10°, 7.5 min), (5°, 10°, 7.5min), (5°, 5°, 7.5min) and (2°, 5°, 7.5min), respectively.

5. Conclusions

The RO plays an important role in sounding of sporadic E layers. As China's first electromagnetic satellite, CSES has already providing service for more than three years up to now. In this study, the Level-1 data of CSES and Wuhan ZLT ionosonde from March 1 to December 1 in 2018 are collected in sounding of sporadic E layers used to study the comparison of heights.

We calculate the geodetic longitude; latitude and elevation of each occultation tangent point in the occultation inversion process, and count the corresponding time information, then extract the CNR data of L1 observations in the occultation inversion period. The occurrence of Es is judged according to the judgment criteria of $|CNR1_i - \overline{CNR1}| > 3std$. Single layer or multi-layer es is judged according to the number of data whose sequence meets the judgment criteria. Combined with the electron density profile of occultation inversion, the correctness of our Es detection algorithm is verified.

According to the Es results we detected, we drew distribution of Es occurrence rate for seasons and altitude, distribution of global Es occurrence rate for seasons. It is concluded that the occurrence height of Es is mainly located at 90-110 km, and there are obvious seasonal and latitudinal changes in the occurrence rate of Es. There is no significant difference in the occurrence frequency of Es in the northern and southern hemispheres in spring and autumn, and it is almost symmetrical along the equator. Summer in the northern hemisphere is the time period of high incidence of Es, and the latitude range of high incidence of Es is 20°-50° in the northern and southern latitudes, mainly around 30°. The period of local time 15:00-18:00 is the high incidence period of Es.

15

Finally, the comparison of the geometric altitudes of sporadic E layers detected in CSES radio occultation profiles and the virtual heights of sporadic E layers obtained by the ZLT ionosonde was carried out with for different space-time matching window, i.e., (10°, 10°, 7.5 min), (5°, 10°, 7.5min), (5°, 5°, 7.5min) and (2°, 5°, 7.5min). For these four windows, the number of CSES matched pairs was 37, 26, 14 and 5, respectively. The correlation coefficients of altitudes were 0.707, 0.736, 0.748 and 0.884, respectively. The comparison of Es altitudes from RO profiles with those from coinciding ground based ionosonde measurements revealed a large correspondence between both measurement techniques.

Data availability

CSES Radio Occultation data can be downloaded from http://www.leos.ac.cn. The Wuhan ZLT ionosonde observations can be downloaded from https://data.meridianproject.ac.cn/.

Author contributions

XL, CX and SG designed the research; CG and JH performed the research; CG, JH and SG analyzed the data; CG drafted the paper. XL, CX and SG put forward valuable modification suggestions. All authors contributed by providing the necessary data and discussions and writing the paper.

Competing interests

The authors declare that they have no conflict of interest.

Acknowledgements

Financial support

References

335   Ambrosi, G., Bartocci, S., Basara, L. **et al.** (2018) The HEPD particle detector of the CSES satellite mission for investigating seismo-associated perturbations of the Van Allen belts, Sci. China Technol. Sci. 61, 643–652, doi:10.1007/s11431-018-9234-9

Arras C, Wickert J, Beyerle G, Heise S, Schmidt T, Jacobi C (2008) A global climatology of ionospheric irregularities derived from GPS radio occultation, Geophys. Res. Lett., 35:L14809. doi:10.1029/2008G L034158

340   Arras C, Wickert J (2017) Estimation of ionospheric sporadic E intensities from GPS radio occultation measurements, J. Atmos. Sol-Terr. Phys., 171:60–63. doi:10.1016/j.jastp.2017.08.006

Axford, W. I.: The formation and vertical movement of dense ionized layers in the ionosphere due to neutral wind shears, J. Geophys. Res., 68, 769–779, 1963. doi:10.1029/JZ068i003p00769

Cao J B, Zeng L, Zhan F, et al. The electromagnetic wave experiment for CSES mission: Search coil magnetometer, Sci.
345   China. Tech. Sci, 2018, 61: 653–658, doi:10.1007/s11431-018-9241-7

Chu YH, Wang CY, Wu KH, Chen KT, Tzeng KJ, Su CL, Feng W, Plane JMC (2014) Morphology of sporadic E layer retrieved from COSMIC GPS radio occultation measurements: wind shear theory examination, J. Geophys. Res., 119:2117–2136. doi:10.1002/2013JA019437

Didebulidze, G. G., Dalakishvili, G., & Todua, M. (2020). Formation of Multilayered Sporadic E under an Influence of
350   Atmospheric Gravity Waves (AGWs), Atmosphere., 11(6), 653. doi: 10.3390/atmos11060653

Gómez-Casco, D., López-Salcedo, J.A. Seco-Granados, G (2018) C/N0 estimators for high-sensitivity snapshot GNSS receivers, GPS Solut., 22, 122. doi:10.1007/s10291-018-0786-y

Gu, S., Dai, C., Fang, W., Zheng, F., Wang, Y., Zhang, Q (2021) Multi-GNSS PPP/INS tightly coupled integration with atmospheric augmentation and its application in urban vehicle navigation, J. Geod., 95(6), –15. doi: 10.1007/s00190-021-
355   01514-8

Gu, S., Wang, Y., Zhao, Q. et al. BDS-3 differential code bias estimation with undifferenced uncombined model based on triple-frequency observation, J. Geod., 94, 45 (2020). doi:10.1007/s00190-020-01364-w

Haldoupis C. (2011) A Tutorial Review on Sporadic E Layers. In: Abdu M., Pancheva D. (eds) Aeronomy of the Earth's Atmosphere and Ionosphere. IAGA Special Sopron Book Series, vol 2. Springer, Dordrecht. doi:10.1007/978-94-007-0326-
360   1_29

Haldoupis, C. (2012) Midlatitude Sporadic E. A Typical Paradigm of Atmosphere-Ionosphere Coupling, Space. Sci. Rev., 168, 441–461. doi:10.1007/s11214-011-9786-8

Hajj, G.A., et al. (2002) A technical description of atmospheric sounding by GPS occultation, J. Atmos. Sol-Terr. Phys., 64.4: doi:10.1016/S1364-6826(01)00114-6

365   Hocke, K., Igarashi, K., Nakamura, M.,Wilkinson, P.,Wu, J., Pavelyev, A., and Wikert, J. (2001): Global sounding of sporadic E layers by the GPS/MET radio occultation experiment, J. Atmos. Solar-Terr. Phys., 63, 1973–1980. doi:10.1016/S1364-6826(01)00063-3

Huang, J. P., Lei, J. G., Li, S. X., Zeren, Z. M., Li, C., Zhu, X. H., Yu, W. H (2018) The Electric Field Detector (EFD) onboard the ZH-1 satellite and first observational results, Earth. Planet. Phys., 2(6), 469–478. doi:10.26464/epp2018045

370   Lei, J., **et al.** (2007) Comparison of COSMIC ionospheric measurements with ground-based observations and model predictions: Preliminary results, J. Geophys. Res., 112, A07308, doi:10.1029/2006JA012240

Lin J, Shen X H, Hu L C, **et al.** (2018) CSES GNSS ionospheric inversion technique, validation and error analysis, Sci. China Tech. Sci., 61: 669–677, doi:10.1007/s11431-018-9245-6

Lou, Y., Luo, X., Gu, S., Xiong, C., Song, Q., Chen, B., **et al.** (2019) Two Typical Ionospheric Irregularities Associated

375   With the Tropical Cyclones Tembin (2012) and Hagibis (2014), ns. J. Geophys. Res. Space. Phys., 124(7), 6237–6252. doi:10.1029/2019JA026861

Luo, J., Wang, H., Xu, X., Sun, F., (2019) The Influence of the Spatial and Temporal Collocation Windows on the Comparisons of the Ionospheric Characteristic Parameters Derived from COSMIC Radio Occultation and Digisondes, Adv. Space Res., 63:3088–3101. doi:10.1016/j.asr.2019.01.024

380   Luo, X., Gu, S., Lou, Y., Cai, L., Liu, Z (2020) Amplitude scintillation index derived from C / N 0 measurements released by common geodetic GNSS receivers operating at 1 Hz, J. Geod., 94(2), 1–14. doi:10.1007/s00190-020-01359-7

Luo, X., Lou, Y., Gu, S., Li, G., Xiong, C., Song, W., Zhao, Z (2021) Local ionospheric plasma bubble revealed by BDS Geostationary Earth Orbit satellite observations, GPS Solut., 25(3), –10. doi:10.1007/s10291-021-01155-6

Mathews J.D.: Sporadic E: current views and recent progress, J. Atmos. Sol.-Terr. Phys. 60, 413 (1998). doi:10.1016/S1364-

385   6826(97)00043-6

Shen, X. H., Zong, Q-G., and Zhang, X. M (2018) Introduction to special section on the China Seismo-Electromagnetic Satellite and initial results. Earth Planet. Phys., 2(6), 439–443. doi:10.26464/epp2018041

Shi, C., Guo, S., Gu, S. et al. Multi-GNSS satellite clock estimation constrained with oscillator noise model in the existence of data discontinuity, J. Geod., 93, 515–528 (2019). doi:10.1007/s00190-018-1178-3

390   Tilo Fytterer,,Christina Arras,,Peter Hoffmann., Christoph Jacobi.(2014). Global distribution of the migrating terdiurnal tide seen in sporadic E occurrence frequencies obtained from GPS radio occultations. Earth, Planets and Space. doi:10.1186/1880-5981-66-79

Tsai, LC., Su, SY., Liu, CH. et al. Global morphology of ionospheric sporadic E layer from the FormoSat-3/COSMIC GPS radio occultation experiment. GPS Solut., 22, 118 (2018). doi:10.1007/s10291-018-0782-2

395   Wang, X., Cheng, W., Zhou, Z., Xu, S., Yang, D., and Cui, J. (2019): Comparison of CSES ionospheric RO data with COSMIC measurements, Ann. Geophys., 37, 1025–1038, doi:10.5194/angeo-37-1025-2019

Whitehead, J. D. (1989), Recent work on mid-latitude and equatorial sporadic-E, J. Atmos. Terr. Phys., 51(5), 401– 424. doi:10.1016/0021-9169(89)90122-0

Whitehead, J. D. (1961), The formation of the sporadic-E layer in the temperate zones, J. Atmos. Terr. Phys., 20, 49– 58. doi:
400   10.1016/0021-9169(61)90097-6

Wickert, J., Pavelyev, A. G., Liou, Y. A., Schmidt, T., Reigber, C., Igarashi, K., Pavelyev, A. A., and Matyugov, S. (2014): Amplitude variations in GPS signals as possible indicator of ionospheric structures, Geophys. Res. Lett., 31, L24801, doi:10.1029/2004GL020607

Wu, D. L., Ao, C. O., Hajj, G. A., de la Torre Juarez, M., and Mannucci, A. J. (2005): Sporadic E morphology from GPS-
405   CHAMP radio occultation, J. Geophys. Res., 110, A01306. doi:10.1029/2004JA010701

Xue Z X, Yuan Z G, Liu K, et al. 2018. Statistical research of Es distribution in inland areas of China based on COSMIC occultation observations. Chinese J. Geophys. (in Chinese), 61(8): 3124-3133. doi:10.6038/cjg2018L0670

Yan, R., Zhima, Z., Xiong, C., Shen, X., Huang, J., Guan, Y., et al. (2020). Comparison of electron density and temperature from the CSES satellite with other space-borne and ground-based observations. J. Geophys. Res. Space. Phys., 125,
410   e2019JA027747. doi:10.1029/2019JA027747

Yeh, W.-H., Huang, C.-Y., Hsiao, T.-Y., Chiu, T.-C., Lin, C.-H., and Liou, Y.-A. (2012): Amplitude morphology of GPS radio occultation data for sporadic-E layers, J. Geophys. Res., 117, A11304. doi:10.1029/2012JA017875

Yeh, W.-H., J.-Y. Liu, C.-Y. Huang, and S.-P. Chen (2014), Explanation of the sporadic-E layer formation by comparing FORMOSAT-3/COSMIC data with meteor and wind shear information, J. Geophys. Res. Atmos., 119, 4568–4579,
415   doi:10.1002/2013JD020798

Yue X, Schreiner W S, Rocken C, et al. Evaluation of the orbit altitude electron density estimation and its effect on the Abel inversion from radio occultation measurements. Radio Sci., 2011, 46: RS1013. doi:10.1029/2010RS004514

Yue, X., Schreiner, W. S., Zeng, Z., Kuo, Y.-H., and Xue, X. (2015): Case study on complex sporadic E layers observed by GPS radio occultations, Atmos. Meas. Tech., 8, 225–236, doi:10.5194/amt-8-225-2015

420   Zhao, Q., Wang, Y., Gu, S. et al. Refining ionospheric delay modeling for undifferenced and uncombined GNSS data processing, J. Geod., 93, 545–560 (2019). doi:10.1007/s00190-018-1180-9

Zhou, X., Yue, X., Liu, H.-L., Lu, X., Wu, H., Zhao, X., & He, J. (2021). A comparative study of ionospheric day-to-day variability over Wuhan based on ionosonde measurements and model simulations, J. Geophys. Res. Space. Phys., 126, e2020JA028589. doi:10.1029/2020JA028589.